Conference on
Transport Phenomena with Moving Boundaries
11th-12th October, Berlin, Germany

THE INFLUENCE OF GAS-LIQUID DENSITY RATIO ON SHAPE AND RISE VELOCITY OF AN ELLIPSOIDAL BUBBLE: A NUMERICAL STUDY BY 3D VOLUME-OF-FLUID COMPUTATIONS

M. WÖRNER

- Forschungszentrum Karlsruhe, Institut für Reaktorsicherheit, Postfach 3640, 76021 Karlsruhe, Germany, E-mail: woerner@irs.fzk.de

Abstract. The present numerical study investigates the influence of the gas-liquid density ratio on bubble shape and bubble Reynolds number (Re_B) by 3D volume-of-fluid computations. For fixed values of the Eötvös number ($Eö_B = 3.06$) and the Morton number ($M = 3.09 \cdot 10^{-6}$) four cases are considered, where the liquid density is 2, 5, 10, and 50 times the gas density. In all cases the ratio of dynamic viscosities is unity. All the simulations result in an oblate ellipsoidal bubble that rises steadily on a rectilinear path. Due to the added mass force the density ratio has a notable influence in the initial stage when the bubble accelerates from rest to its terminal velocity. Once the bubble reached its terminal velocity, the dependence of the bubble Reynolds number and the ellipse ratio on the density ratio are very weak. The computed value for Re_B agrees well with a relation derived from two-fluid wave theory that expresses Re_B as function of $Eö_B$ and M.

Keywords. ellipsoidal bubble, bubble rise velocity, bubble Reynolds number, density ratio, similitude analysis, volume-of-fluid method.

INTRODUCTION

Using the volume-of-fluid (VOF) method for tracking the gas-liquid interface, we recently performed three-dimensional (3D) direct numerical simulations of single bubbles rising in a channel formed by two parallel vertical plates filled with a quiescent liquid [9-11]. In these simulations the gas-liquid viscosity ratio was $\Gamma_\mu = \mu_g^* / \mu_l^* = 1$ while the gas-liquid

density ratio was $\Gamma_\rho = \rho_g^* / \rho_l^* = 0.5$. Here, the indices *g* and *l* denote the gas and liquid phase, respectively, and * is used to indicate a dimensional quantity. The value for the ratio of densities was chosen in favor of a lower one to reduce the CPU time. As will be discussed below, the maximum time step size allowed for numerical stability of our explicit time integration scheme decreases almost linear with decreasing Γ_ρ. Though the simulations were run with $\Gamma_\rho = 0.5$, the CPU time required was still up to 100 hours for a simulation run.

The simulations presented in [9-11] were performed for four different combinations of Morton number (*M*) and bubble Eötvös number ($Eö_B$). These non-dimensional numbers are defined as

$$M \equiv \frac{\left(\rho_l^* - \rho_g^*\right) g^* \mu_l^{*4}}{\rho_l^{*2} \sigma^{*3}}, \quad Eö_B \equiv \frac{\left(\rho_l^* - \rho_g^*\right) g^* d_V^{*2}}{\sigma^*}.$$

Here g^* denotes the acceleration of gravity, σ^* is the coefficient of surface tension, and d_V^* is the volume-equivalent diameter of the bubble. The combinations of (M, $Eö_B$) were chosen so that according to the diagram given in the book of Clift, Grace, and Weber (CGW) [4, p. 27] a spherical, ellipsoidal, oblate spherical cap, and a wobbling bubble shape should be expected. In this diagram the bubble Reynolds number (Re_B) is displayed as function of (M, $Eö_B$), where $Re_B \equiv \rho_l^* d_V^* U_T^* / \mu_l^*$ and U_T^* is the terminal rise velocity of the bubble. In the experiments used by CGW to deduce this diagram, the gas density is typically three orders of magnitude lower than the liquid one. Though in our simulations the density ratio is 0.5, the Reynolds number, shape, rising path, and wake type of the bubble agreed qualitatively very well with the diagram of CGW for all four different combinations of (M, $Eö_B$).

For a bubble rising with its terminal velocity through an infinite liquid the physical quantities of influence are included in the following equation [5]:

$$F^*\left(g^*, \rho_l^*, \mu_l^*, \sigma^*, \rho_g^*, \mu_g^*, d_V^*, U_T^*\right) = 0. \tag{1}$$

Similitude analysis shows that the above equation may be rewritten in terms of five independent dimensionless groups [3,5]. For example, the bubble Reynolds number, which may be interpreted as non-dimensional bubble terminal rise velocity, is a function of Morton number, of bubble Eötvös number, and of the ratios of densities and dynamic viscosities:

$$Re_B = f\left(M, Eö_B, \Gamma_\rho, \Gamma_\mu\right). \tag{2}$$

Grace [5] noted that for bubbles rising in liquids Γ_ρ and Γ_μ tend to be very small so that the density and viscosity of the dispersed phase become unimportant and $Re_B = f(M, Eö_B)$. Clift et al. [4, p. 173] compare experimental results obtained by different workers for Re_B as a function of $Eö_B$ for systems with essentially the same Morton number ($M \approx 2 \cdot 10^{-10}$) but

widely different values of Γ_μ (0.35 to 20). Though the data exhibit some scatter it is evident that Re_B does not vary systematically with Γ_μ.

Due to the close agreement we observed between Re_B in our simulations (performed with $\Gamma_\rho = 0.5$) and the diagram of CGW (deduced from experiments with $\Gamma_\rho \approx 0.001$) for fixed values of ($M$, $Eö_B$) one may conjecture that the dependence of the bubble Reynolds number on the density ratio is weak at all, not only for $\Gamma_\rho << 1$. While there are a number of studies addressing the influence of the viscosity ratio on the flow in and outside a bubble or droplet there exist only few papers investigating the influence of the density ratio. Two numerical studies are that of Chen et al. [2] and Juncu [6]. In both papers together with the density ratio also the Eötvös number and Morton number are varied. This procedure is, however, unsuited to reveal the specific functional dependence of Re_B on Γ_ρ expressed by Eq. (2).

The purpose of the present paper is to investigate the influence of the density ratio on the shape and on the rise velocity of a single bubble in a systematic manner. We restrict ourselves to the parameters ($M = 3.09 \cdot 10^{-6}$, $Eö_B = 3.06$) which corresponds to an ellipsoidal bubble that rises steadily on a rectilinear path. In the simulations, beside the values for M and $Eö_B$, also the value for the viscosity ratio is fixed ($\Gamma_\mu = 1$). So the only parameter on the right-hand-side of Eq. (2) which we vary is the density ratio. In particular, we perform simulations where the liquid density is 2, 5, 10, and 50 times the gas density.

The paper is organized as follows. In the next section we present the governing equations, the numerical method, and the parameters of the simulations. In the following section we discuss the results, where we focus on the dependence of bubble Reynolds number and bubble shape on the density ratio. The papers closes with the conclusions.

SIMULATION METHOD

Governing equations

In this section we present the governing equations of our volume-of-fluid method. To obtain non-dimensional equations the following scaling is introduced

$$\vec{x} = \begin{pmatrix} x \\ y \\ z \end{pmatrix} = \frac{\vec{x}^*}{L^*_{ref}}, \vec{u} = \frac{\vec{u}^*}{U^*_{ref}}, t = \frac{t^* U^*_{ref}}{L^*_{ref}}, \rho = \frac{\rho^*}{\rho^*_l}, \mu = \frac{\mu^*}{\mu^*_l}, P = \frac{p^* - \rho^*_l \vec{g}^* \cdot \vec{x}^*}{\rho^*_l {U^*_{ref}}^2},$$

where L^*_{ref} and U^*_{ref} are a reference length and reference velocity, respectively. Note that in the formulation of the non-dimensional pressure we include the hydrostatic pressure of the liquid phase. Due to this, in the momentum equation the buoyancy force will appear instead of

the gravity force. In non-dimensional form this brings the Eötvös number into play instead of the Froude number, which in the context of Eq. (2) is of certain advantage here. With the above normalization, the non-dimensional volume-averaged continuity equation is given by

$$\nabla \cdot \vec{u}_m = 0, \tag{3}$$

while the non-dimensional volume-averaged Navier-Stokes equation is given by

$$\frac{\partial \rho_m \vec{u}_m}{\partial t} + \nabla \cdot \rho_m \vec{u}_m \vec{u}_m = -\nabla P + \frac{1}{Re_{ref}} \nabla \cdot \mu_m \left(\nabla \vec{u}_m + \left(\nabla \vec{u}_m \right)^{\mathrm{T}} \right) - (1-f) \frac{E\ddot{o}_{ref}}{We_{ref}} \frac{\vec{g}^*}{g^*} + \frac{\kappa \vec{n} a_{int}}{We_{ref}}. \tag{4}$$

In the latter two equations $\vec{u}_m$ is the non-dimensional center of mass velocity

$$\vec{u}_m \equiv \frac{1}{U^*_{ref}} \frac{f \rho^*_l \vec{u}^*_l + (1-f) \rho^*_g \vec{u}^*_g}{f \rho^*_l + (1-f) \rho^*_g},$$

where f is the liquid volumetric fraction within the averaging volume V, and ρ_m and μ_m are the non-dimensional mixture density and viscosity, respectively,

$$\rho_m \equiv \frac{f \rho^*_l + (1-f) \rho^*_g}{\rho^*_l}, \quad \mu_m \equiv \frac{f \mu^*_l + (1-f) \mu^*_g}{\mu^*_l}.$$

The last term in Eq. (4) expresses the effect of surface tension. There, κ is the interface curvature, $\vec{n}$ is the unit normal vector to the interface, and a_{int} is the interfacial area concentration within the mesh volume. The definitions of the reference Reynolds number (Re_{ref}) and reference Eötvös number ($E\ddot{o}_{ref}$) appearing in Eq. (4) are equivalent to the respective one of Re_B and $E\ddot{o}_B$ given above, but where U^*_T is replaced by U^*_{ref} and d^*_V is replaced by L^*_{ref}. The definition of the reference Weber number (W_{ref}) is

$$We_{ref} \equiv \frac{\rho^*_l L^*_{ref} {U^*_{ref}}^2}{\sigma^*}.$$

Note that the Morton number is correlated to the Reynolds, Eötvös, and Weber numbers by

$$M = \frac{E\ddot{o}_{ref} We^2_{ref}}{Re^4_{ref}} = \frac{E\ddot{o}_B We^2_B}{Re^4_B}.$$

The set of equations is completed by the transport equation for the liquid volumetric fraction

$$\frac{\partial f}{\partial t} + \nabla \cdot \left(f \vec{u}_m \right) = 0. \tag{5}$$

The derivation of the above set of volume-averaged volume-of-fluid equations is given in [15]. The form of Eqs. (3) and (4) as given above already implies that within volume V both phases share the same pressure and the same velocity. The latter assumption corresponds to a locally homogeneous model. Equations (3) and (4) do not account for contamination of the interface by surfactants. The results to be presented thus correspond to a “pure” system.

Numerical method

For the solution of the *f*-equation (5) by the VOF method we have developed a new algorithm called EPIRA (Exact Plane Interface Reconstruction Algorithm) [9,11], which belongs to the class of PLIC (Piecewise Linear Interface Calculation) methods. EPIRA reconstructs a plane 3D interface correctly, regardless of its orientation. The EPIRA algorithm has been implemented in our in-house computer code TURBIT-VOF [9], which solves the non-dimensional continuity and Navier-Stokes equations (3) and (4) together with the *f*-equation (5). TURBIT-VOF is designed to simulate flows in plane channels. It employs a staggered grid, uniform in the *x*- and *y*-directions (parallel to the walls), but possibly non-uniform in *z*-direction (normal to the walls). A second order central difference scheme is used to discretize the diffusive and non-linear convective terms in the Navier-Stokes equation. For discretization of the surface tension term we refer to [11]. The solution algorithm in TURBIT-VOF is based on a projection method. Starting from the results at time level *n*, a predictor step is performed by an explicit third order Runge-Kutta time integration scheme where the pressure term is neglected. This yields an intermediate non-solenoidal velocity field. In the corrector step this intermediate velocity field is projected to the divergence free velocity field $\vec{u}_m^{n+1}$ at the new time level *n* +1. As the pressure is treated implicitly, the corrector step requires the solution of a pressure Poisson equation. This is done by a conjugate gradient method. For further details of the numerical method as well as for verification of the code by several benchmark problems we refer to [9,11].

Computational grid, boundary conditions, and initial conditions

Figure 1 shows the coordinate system and a sketch of the computational domain. The *x*-, *y*- and *z*-axes were assigned in vertical direction, in transverse direction, and in wall-normal direction, respectively. The gravity vector points in negative *x*-direction. In *x*- and *y*-direction we have periodic boundary conditions; at $z = 0$ and $z = 1$ we have rigid walls and no-slip boundary conditions. The size of the computational domain is $L_x^* \times L_y^* \times L_z^* = 2\,L_{ref}^* \times L_{ref}^* \times L_{ref}^*$. This domain is discretized by 128 × 64 × 64 uniform mesh cells resulting in $\Delta x = \Delta y = \Delta z = 0.015625$. At time $t = 0$ a spherical bubble of diameter $d_V^* = L_{ref}^* / 4$ is positioned in the domain with its center located at (0.5,0.5,0.5). The diameter of the bubble is resolved by 16 mesh cells. The overall void fraction is about 0.4 %. Both, the liquid and gas are initially at rest.

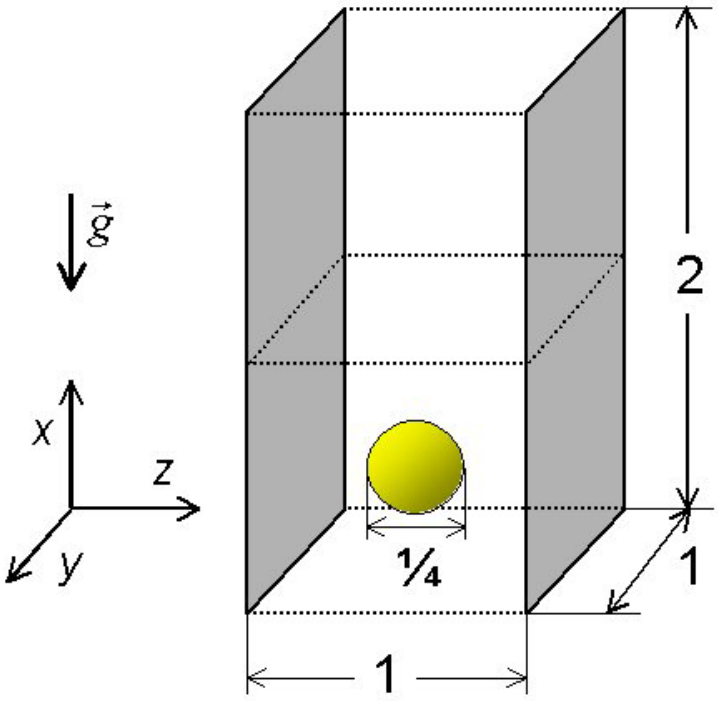

Fig. 1: Sketch of coordinate system and computational domain.

Due to the lateral walls and because we use periodic boundary conditions in the *x*- and *y*-direction, the physical quantities of influence given in Eq. (1) are no longer complete and do not fully characterize the problem. While the only length scale in Eq. (1) is the bubble diameter, we have now three additional length scales due to our finite computational domain, namely L_x^*, L_y^*, L_z^*. Thus, the non-dimensional groups as given by Eq. (2) which apply to a single bubble rising in an infinite fluid should be extended by $d_V^*/L_x^*, d_V^*/L_y^*, d_V^*/L_z^*$. One can, however, argue that with the hydraulic diameter $d_h^* = 2L_{ref}^*$ the ratio d_V^*/d_h^* takes a value of 0.125 and thus the wall influence is already small [4, p. 233]. Furthermore, we will restrict our analysis to the stage when the interaction with the "leading" and "trailing" bubble is small and thus stop the simulations when the bubble has risen a vertical distance of about half of the height of the computational domain. The results should then be comparable to that of a single bubble and altogether the influence of $d_V^*/L_x^*, d_V^*/L_y^*, d_V^*/L_z^*$ should be small.

Parameters of the simulations

To set up the simulations we must specify the reference quantities Re_{ref}, $Eö_{ref}$, and We_{ref} in the Navier-Stokes equation (4). We proceed as follows. We consider fixed values for the Morton number ($M = 3.09 \cdot 10^{-6}$), the bubble Eötvös number ($Eö_B = 3.06$), and the viscosity

ratio ($\Gamma_\mu = 1$) and set $L^*_{ref} = 4\,\mathrm{m}$, $U^*_{ref} = 1\,\mathrm{ms}^{-1}$, $g^* = 9.81\ \mathrm{ms}^{-2}$. The only parameter we vary is the density ratio Γ_ρ. Based on the values given above we can successively compute

$$Eö_{ref} = \left(\frac{L^*_{ref}}{d^*_V}\right)^2 Eö_B, \quad We_{ref} = \frac{Eö_{ref}}{1-\Gamma_\rho}\frac{U^{*\,2}_{ref}}{g^* L^*_{ref}}, \quad Re_{ref} = \left(\frac{Eö_{ref} We^2_{ref}}{M}\right)^{0.25}.$$

In Table 1 we give the input values Re_{ref}, $Eö_{ref}$, and We_{ref} for the different density ratios considered in the present study. Additionally, we give the values of We_{ref} and Re_{ref} for the asymptotic case $\Gamma_\rho \to 0$. It is important to note that in our simulations we do not specify any explicit values for the fluid properties $\rho^*_l, \mu^*_l, \sigma^*, \rho^*_g, \mu^*_g$. From similitude analysis, however, we know that the computed results are valid for any combination of fluid properties that results in the values of M, $Eö_B$, Γ_ρ, and Γ_μ used in the respective simulation run.

Tab. 1: Parameters of the simulations for different values of the density ratio.

Run	Γ_ρ	$1/\Gamma_\rho$	$Eö_{ref}$	We_{ref}	Re_{ref}	Δt	N_t
R2	0.5	2	49.05	2.5	100.0	0.0005	1,100
R5	0.2	5	49.05	1.5625	78.898685	0.0003	1,800
R10	0.1	10	49.05	1.3888	74.386394	0.00015	3,200
R50	0.02	50	49.05	1.2755	71.285586	0.00003	13,000
	0	∞	49.05	1.25	70.56913		

Time step restrictions

In the predictor step of our solution algorithm we use an explicit time integration scheme. Therefore we have to meet certain criteria to ensure the numerical stability of the method. These criteria result from the different forces in the Navier-Stokes Eq. (4), i.e. from convective, viscous, buoyancy, and capillary forces. For a uniform grid the non-dimensional convective (Δt_{CFL}) and viscous (Δt_μ) time step criteria are

$$\Delta t_{CFL} = \frac{\Delta x}{\max\limits_{i,j,k}\left|\vec{u}^{\,n}\right|}, \quad \Delta t_\mu = \frac{1}{6}\Delta x^2\, Re_{ref}\, \min\left(1, \frac{\Gamma_\rho}{\Gamma_\mu}\right), \tag{6}$$

while that ones due to buoyancy forces (Δt_g) [12] and capillary forces (Δt_σ) [1] are

$$\Delta t_g = 2\Delta x\left(\max_{i,j,k}\left|\vec{u}^{\,n}\right| + \sqrt{\left(\max_{i,j,k}\left|\vec{u}^{\,n}\right|\right)^2 + \frac{4\Delta x}{\Gamma_\rho}\left|\frac{Eö_{ref}}{We_{ref}}\right|}\right)^{-1}, \quad \Delta t_\sigma = \sqrt{\frac{\Delta x^3}{4\pi} We_{ref}\left(1+\Gamma_\rho\right)}. \tag{7}$$

The maximum time step size allowed is $\Delta t_{max} = \min\left(\Delta t_{CFL}, \Delta t_{\mu}, \Delta t_{g}, \Delta t_{\sigma}\right)$. The above four criteria are derived by considering the respective force alone. They do not take into account the nonlinear character of the Navier-Stokes equation. Therefore we determine the value of Δt that will be actually used in the computations by multiplying Δt_{max} by a safety factor. In the simulations to be presented here this safety factor is about 0.5.

In Figure 2 we show the four time step criteria for different values of the inverse of the density ratio. The parameters in Eqs. (6) and (7) are as given above. From our previous simulations [9,11] the value of the maximum velocity is guessed to $\max_{i,j,k}\left|\vec{u}^{n}\right| = 4$. Figure 2 shows that for a density ratio $\Gamma_{\rho}^{-1} \leq 4$ the most restrictive criterion is the one due to surface tension while for $\Gamma_{\rho}^{-1} > 4$ it is the one due to viscous forces. By Eq. (6) it is evident that Δt_{μ} increases linearly with Γ_{ρ}, or as is displayed in Fig. 2, decreases linearly with increasing $1/\Gamma_{\rho}$.

The time step used in the simulations and the number of time steps computed (N_t) are given in Table 1. The simulations were run on a single processor of a Siemens Fujitsu VPP 5000 parallel vector computer. For the present grid which consists of 524,288 mesh cells in one hour of CPU time about 200 time steps are computed. Thus, only the run for $\Gamma_{\rho} = 0.02$ took about 60 hours of CPU time. Therefore with our current method, which treats the viscous term explicitly, we can not afford to perform simulations with Γ_{ρ} much smaller than 1/50.

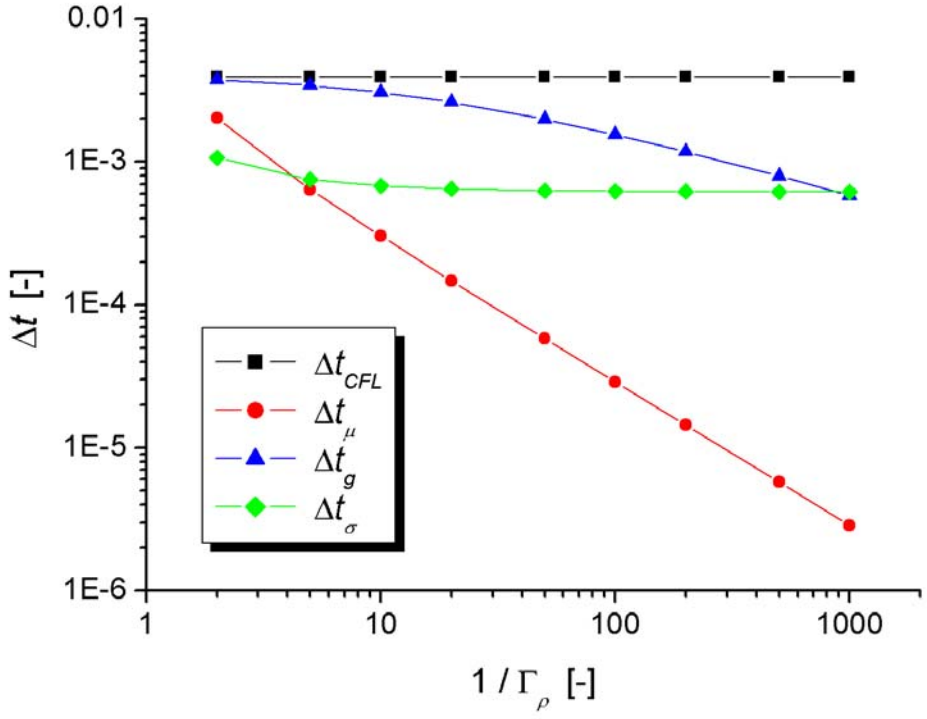

Fig. 2: Time step limitation due to different forces as function of inverse of density ratio.

RESULTS

To give a first impression on the computed flow field, we show in Figure 3 a visualization of the bubble shape and the velocity field in plane $y = 0.5$ for simulation run R50. The visualization is for time $t = 0.381$ where the vertical coordinate of the bubble center of mass is $x_{com} = 1.5$. Thus, the bubble has risen vertically a distance of four times of its equivalent diameter. From the left part of Figure 3 it can be seen that the bubble obeys a closed wake. From the magnified detail in the right part of Figure 3 it becomes evident that the bubble has an oblate ellipsoidal shape.

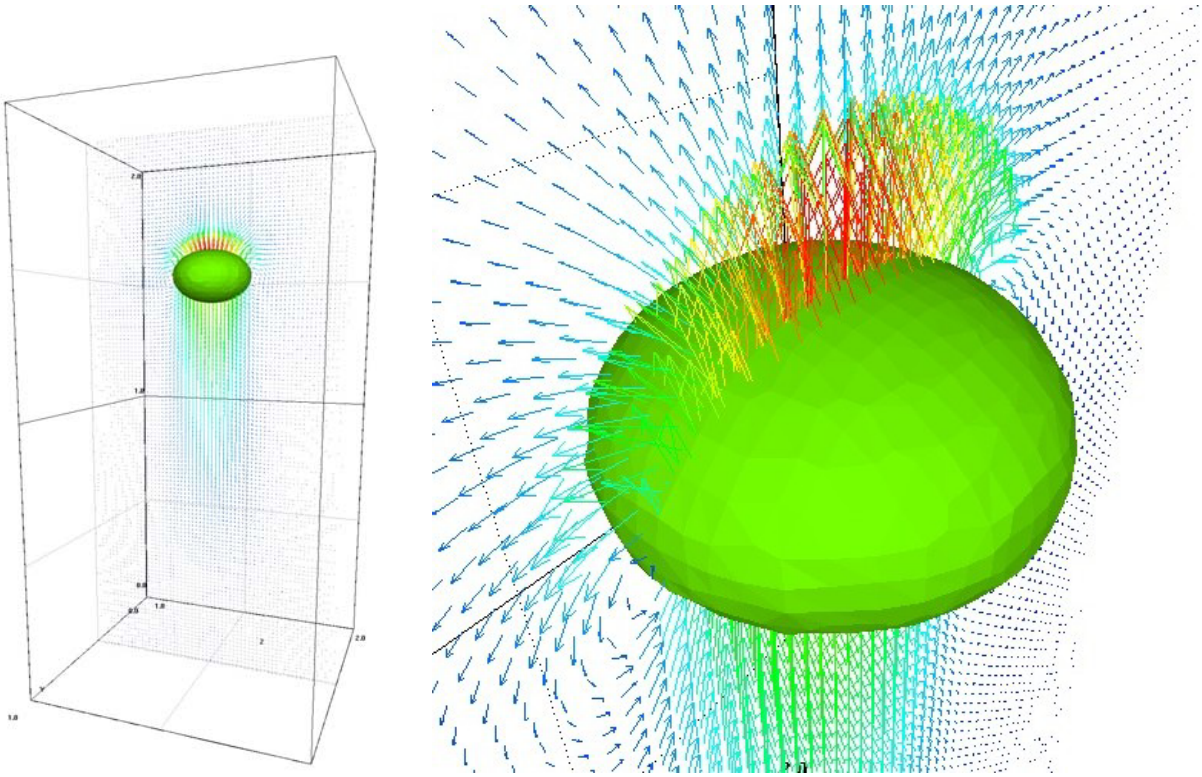

Fig. 3: Instantaneous bubble surface and velocity vectors in plane $y = 0.5$ for run R50.

Bubble rise path

In all the runs the bubbles rise along a vertical rectilinear path. The maximum lateral deviations from this rectilinear path are less than 0.1% of L^*_{ref}. In Figure 4 the vertical coordinate of the bubble's center of mass, $x_{com}(t)$, is displayed for the different runs. It is evident that for each density ratio two distinct temporal ranges do exist. In the initial range the bubble's center of mass accelerates and $x_{com}(t) \propto C_1 t^2$. This initial range is followed by a second range where the bubble rises steadily and $x_{com}(t) \propto C_2 t$.

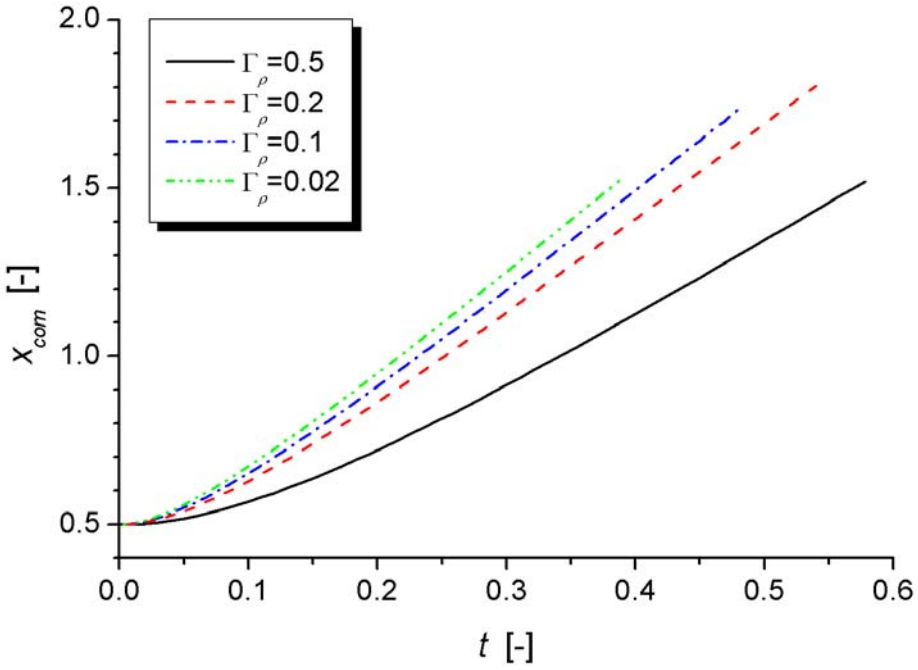

Fig. 4: Computed vertical position $x_{com}(t)$ of bubble center of mass for different density ratios.

Figure 4 shows that the lower Γ_ρ the shorter the first range and the higher the coefficient C_1. This observation can be explained as follows. In the first stage of bubble rise we expect a balance between the sum of the unsteady and inertial term and the buoyancy term. Neglecting the other terms, we can simplify the momentum equation (4) and write it in the following non-conservative form

$$\rho_m \frac{D\vec{u}_m}{Dt} = \rho_m \left(\frac{\partial \vec{u}_m}{\partial t} + \vec{u}_m \cdot \nabla \vec{u}_m \right) = -(1-f) \frac{E\ddot{o}_{ref}}{We_{ref}} \frac{\vec{g}^*}{g^*}.$$

While the above equation is local we are interested here in the global behaviour of the bubble, i.e. the behaviour of the entire region where $f = 0$. Considering only the x-component of the above equation we approximate $u_{m,x}$ by the bubble rise velocity U_B. To account for the added mass force, we approximate the mixture density by $\rho_m \approx \left(\rho_g^* + C_{AM}\rho_l^*\right)/\rho_l^*$. Taking the theoretical value for a spherical bubble, $C_{AM} = 0.5$, and replacing $U_B = Dx_{com}/Dt$ in the above equation we obtain the following ordinary differential equation for $x_{com}(t)$

$$\frac{D^2 x_{com}}{Dt^2} = \frac{1}{\frac{1}{2} + \Gamma_\rho} \frac{E\ddot{o}_{ref}}{We_{ref}} = 2\frac{1-\Gamma_\rho}{1+2\Gamma_\rho} \frac{g^* L_{ref}^*}{U_{ref}^{*\,2}}.$$

Integrating twice and setting the integration constants properly, we obtain

$$x_{com}(t) = 0.5 + \frac{1-\Gamma_\rho}{1+2\Gamma_\rho} \frac{g^* L_{ref}^*}{U_{ref}^{*\,2}} t^2 = 0.5 + C_1(\Gamma_\rho) t^2.$$

In Table 2 we give the values of $C_1(\Gamma_\rho)$ for the different density ratios, while in Figure 5 we compare the computed results for $x_{com}(t)$ - 0.5 with the parabola $C_1(\Gamma_\rho)\, t^2$ for the different runs. Note that x_{com} is not displayed for each time step, but only for those time steps for which the simulation data are saved on a restart file. This is typically done in intervals of 20 to 200 time steps, depending on the size of Δt. From Figure 5 it can be seen that the coefficient C_1 deduced by the above simple considerations does very well describe the dependence of x_{com} in the initial stage of bubble rise ($t \leq 0.04$). However, the rise velocity is overestimated slightly in a systematic manner. This slight overestimation can be explained by the fact that in our derivation we neglected viscous forces. As becomes evident from Figure 5, the results for R50 are already very close to the parabola for the limit case of $\Gamma_\rho = 0$.

Tab. 2: Coefficient $C_1(\Gamma_\rho)$ for different values of the density ratio.

Run	Γ_ρ	$1 / \Gamma_\rho$	$(1-\Gamma_\rho)/(1+2\Gamma_\rho)$	C_1
R2	0.5	2	0.25	9.81
R5	0.2	5	0.5714	22.42
R10	0.1	10	0.75	29.43
R50	0.02	50	0.9423	36.98
	0	∞	1	39.24

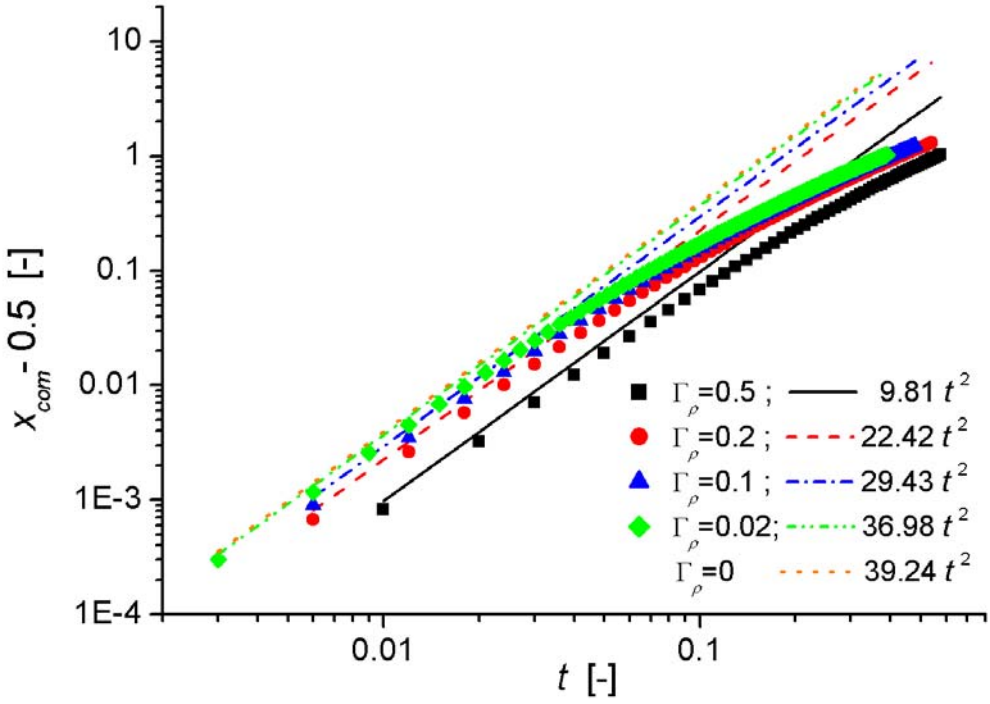

Fig. 5: Comparison of computed values of $x_{\mathrm{com}}(t)$ (symbols) with parabola $C_1(\Gamma_\rho)t^2$ (lines) for the different runs in double-logarithmic representation.

Bubble rise velocity

We now consider the second range in Figure 4, where the bubble rises steadily and where we find a linear dependence of x_{com} on t. Our main interest is how the bubble Reynolds number depends on the density ratio. The bubble Reynolds number can be evaluated via relation

$$Re_B = \frac{d_V^*}{L_{ref}^*}\frac{U_B^*}{U_{ref}^*} Re_{ref} = \frac{1}{4} U_B \, Re_{ref} ,$$

where U_B is the time derivative of $x_{com}(t)$. The temporal evolution of Re_B for the different runs is displayed in Figure 6. We see that the curves for runs R5, R10, and R50 almost coincide for $t > 0.3$. Also run R2 seems to approach the same value of Re_B which is about 56. In the inset graphic in Figure 6 it can be seen that for all runs Re_B is still slightly increasing and has not yet reached its saturation value. Nevertheless, we decided not to continue the simulations. Due to the periodic boundary conditions the results might otherwise be no longer representative for the rise of a single bubble but for the rise of a chain of periodically released bubbles. Also due to the interaction of the bubble with the wake of the leading bubble instabilities may be triggered which may cause a non-rectilinear path. Note that the rectilinear path as well as the value of $Re_B \approx 56$ computed here for a bubble with $E\ddot{o}_B = 3.06$ and $M = 3.09 \cdot 10^{-6}$ agree well with experimental observations for similar values of ($E\ddot{o}_B$, M) [4].

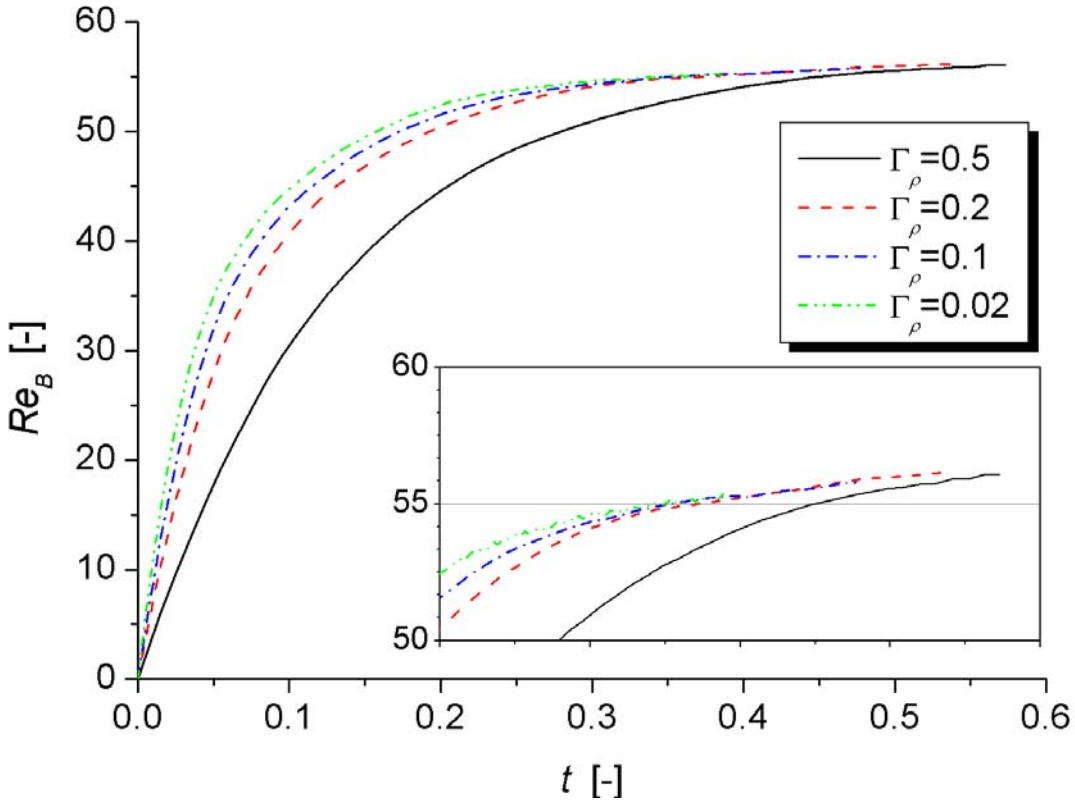

Fig. 6: Temporal evolution of bubble Reynolds number for different density ratios.

We now compare the results obtained for the bubble Reynolds number with an analytical approach. By analogy to two-fluid wave theory, which yields an expression for the phase velocity of inviscid surface tension and gravity waves at a free surface, Mendelson [8] proposed the following formula for the terminal rise velocity of a bubble in the surface-tension or buoyancy force dominated regime

$$U_T^* = \sqrt{\frac{2\sigma^*}{\rho_l^* d_V^*} + \frac{g^* d_V^*}{2}} .$$

While Mendelson noted that the only justification for the above equation is how well it correlates experimental data, Marrucci et al. [7] extended the formula for liquid-liquid systems (i.e. a dispersed liquid drop rising in an immiscible continuous liquid) and proposed

$$U_T^* = \sqrt{\frac{2\sigma^*}{\rho_l^* d_V^*} + \frac{g^* d_V^* \Delta\rho^*}{2\rho_l^*}} . \tag{8}$$

Here, $\Delta\rho^*$ is the difference between the densities of the continuous and dispersed phase. Recently, Tomiyama et al. [13] gave a physical interpretation of Eq. (8). They noted that multiplying Eq. (8) by $\rho_l^* d_V^* / \mu_l^*$ yields

$$Re_B = \left(2 + \frac{1}{2} E\ddot{o}_B\right)^{0.5} \left(\frac{E\ddot{o}_B}{M}\right)^{0.25} . \tag{9}$$

Thus, Re_B is a function of $E\ddot{o}_B$ and M but does not depend on Γ_ρ and Γ_μ. For the values $E\ddot{o}_B$ = 3.06 and $M = 3.09 \cdot 10^{-6}$ equation (9) gives $Re_B = 59.3$. Thus, the value $Re_B \approx 56$ obtained in the present computational study agrees well with the above theory. Finally, we remark that from equation (9) a rather simple expression for the drag coefficient results [13], which turns out to be a function of the bubble Eötvös number alone, namely

$$C_D \equiv \frac{4}{3} \frac{d_V^* g^* \Delta\rho^*}{\rho_l^* U_T^{*2}} = \frac{4}{3} \frac{E\ddot{o}_B}{We_B} = \frac{4}{3} \sqrt{\frac{E\ddot{o}_B^3}{M\, Re_B^4}} = \frac{8}{3} \frac{E\ddot{o}_B}{E\ddot{o}_B + 4} .$$

Bubble shape

In all the present simulations the bubble takes the shape of an ellipsoid. There is no strict fore-aft symmetry, but the bubble is slightly more flat at its top than at its rear. To quantitatively compare the bubble shape for the runs with different density ratio, we evaluated the three dimensions a_x, a_y, a_z of the bubble at that instant in time when $x_{com} = 1.5$. We found that in each case the ratio a_z/a_y takes a value between 0.99 and 1. Thus, the bubble is rotationally symmetrical and the lateral walls are obviously sufficiently far away so that they

do not affect the bubble shape. The ratios a_x/a_y and a_x/a_z take values between 0.64 and 0.66 in the different runs. With decreasing Γ_ρ we observe a small tendency to higher values.

Based on experiments for fifty-four dispersed-continuous phase systems Wellek et al. [14] derived empirical relations for the height-to-width ratio (E) of non-oscillating bubbles and drops, over a wide range of particle Reynolds numbers. They obtained the relation

$$E = \left(1 + 0.163 E\ddot{o}_B^{0.757}\right)^{-1}, \tag{10}$$

which is valid for $E\ddot{o}_B < 40$ and $M \le 10^{-6}$. Though the Morton number $M = 3.09 \cdot 10^{-6}$ considered in our numerical study is slightly out of the range for which the latter correlation was derived we note that for $E\ddot{o}_B = 3.06$ correlation (10) yields a value of 0.72. So the bubble in our computations is with a value of $E \approx 0.66$ distinctively more oblate than relation (10) would suggest. However, relation (10) was obtained for contaminated systems whereas our simulations correspond to a pure system. It is well known [4, p. 182] that bubbles and drops in pure systems are significantly more deformed than corresponding fluid particles in contaminated systems.

CONCLUSIONS

A numerical study is presented in which the influence of the gas-liquid density ratio (Γ_ρ) on bubble shape and bubble Reynolds number (Re_B) is investigated. For fixed values of the bubble Eötvös number ($E\ddot{o}_B = 3.06$) and the Morton number ($M = 3.09 \cdot 10^{-6}$) and for a unity viscosity ratio we performed 3D volume-of-fluid computations for four different cases, where the liquid density is 2, 5, 10, and 50 times the gas density. All the simulations result in an oblate ellipsoidal bubble that rises steadily along a rectilinear path. The results indicate that due to the added mass force the density ratio has a notable influence on how fast the bubble accelerates from rest to its terminal velocity. Once the bubble reached its terminal velocity, however, the functional dependence of both, the bubble Reynolds number and the bubble's height-to-width ratio on the density ratio appears to be very weak. With decreasing Γ_ρ the temporal evolution of the vertical coordinate of the bubbles center of mass converges to the curve of the limiting case $\Gamma_\rho \to 0$. The results obtained for liquid-to-gas density ratio 50 are already very close to the results to be expected for the asymptotic case $\Gamma_\rho \to 0$. For all the four cases the value of Re_B is about 56. This value agrees well with a relation derived by two-phase wave theory. In this relation Re_B depends on $E\ddot{o}_B$ and M but does not depend on Γ_ρ and Γ_μ. For the values of $E\ddot{o}_B$ and M considered here it yields $Re_B = 59.3$.

By the results obtained we conclude that for an ellipsoidal bubble rising steadily on a rectilinear path the bubble shape and non-dimensional terminal rise velocity, expressed by the

bubble Reynolds number, are not notably affected by the gas-to-liquid density ratio as long as there is similarity of $Eö_B$, M and Γ_μ. At present this result is demonstrated only for the specific parameters of $Eö_B$, M, and Γ_μ given above. However, the good agreement with two-phase wave theory indicates that a similar conclusion may also hold for other values of $Eö_B$ and M as long as the bubble is in the surface tension or buoyancy dominated regime (as opposed to the viscous regime) and rises steadily on a rectilinear path. For this kind of bubbles then rather universal relations for bubble Reynolds number and drag coefficient in terms of $Eö$ and M should exist. So, the correlations for the drag coefficient given in [13] which were verified by experiments where $\Gamma_\rho \approx 0.001$ may in fact be applicable to gas-liquid or liquid-liquid systems of any density ratio.

The present findings are not directly verified by experiments yet. To verify them it would be necessary to perform experiments with at least two sets of different gas-liquid or liquid-liquid systems which obey the same Morton number but a significantly different density ratio. If there is similarity in the Morton number, then similarity in the Eötvös number can easily be ensured by properly setting the bubble diameters. It may be more difficult to ensure similarity of the viscosity ratio of the different gas-liquid or liquid-liquid systems. However, as discussed in the introduction, there is experimental evidence that for a fixed Morton number the influence of the viscosity ratio on the bubble Reynolds number is small.

Up to now we restricted our attention to the influence of the density ratio on the bubble shape and the rise velocity of the bubble's center of mass. In future work we will perform a detailed comparison of the exterior and interior flow fields for runs with different density ratios. If similarity holds for the exterior flow field, hopefully, rather universal models for the turbulence induced by bubbles rising almost steadily in dilute gas-liquid flows may be derived in terms of $Eö_\mathrm{B}$ and M. Furthermore, such a kind of similarity may allow to perform computationally efficient VOF simulations with density ratio of order 0.1 while the results may be of relevance for gas-liquid systems with density ratio of order 0.001, at least as regards to steadily rising bubbles.

ACKNOWLEGEMENTS

The author thanks Dr. W. Sengpiel, Dr. G. Grötzbach, and B. Ghidersa for useful suggestions and discussions and for carefully reading the manuscript.

NOMENCLATURE

Latin symbols

a_{int}	interfacial area concentration
a_x, a_y, a_z	dimensions of bubble
C_D	drag coefficient
d_B	bubble diameter
d_h	hydraulic diameter
E	height-to-width ratio of bubble
$Eö$	Eötvös number
f	liquid volumetric fraction
g	gravity
L	length
M	Morton number
$\vec{n}$	interface normal vector
P	pressure
Re	Reynolds number
t	time
Δt	time step size
$\vec{u}, U$	velocity
V	averaging volume
We	Weber number
x, y, z	Cartesian coordinates
Δx, Δy, Δz	mesh size

Greek symbols

Γ_μ	gas-liquid viscosity ratio
Γ_ρ	gas-liquid density ratio
κ	interface curvature
μ	dynamic viscosity
ρ	density
σ	coefficient of surface tension

Subscripts

B	bubble
CFL	Courant-Friedrichs-Lewy
com	center of mass
g	gas
l	liquid
m	mixture quantity
ref	reference value
T	terminal value
V	volume-equivalent

Superscripts

n	discrete time level
T	transposed
*	dimensional quantity
$\rightarrow$	vector

REFERENCES

[1] Brackbill, J.U., Kothe, D.B., Zemach, C.: A Continuum Method for Modelling Surface Tension. J. Comput. Phys. 100 (1992) 335-354.

[2] Chen, L., Garimella, S.V., Reizes, J.A., Leonardi, E.: The development of a bubble rising in a viscous liquid. J. Fluid Mech. 387 (1999) 61-96.

[3] Churchill, S.W.: A Theoretical Structure and Correlating Equation for the Motion of Single Bubbles. Chem. Eng. Process. 26 (1989) 269-279.

[4] Clift, R., Grace, J.R., Weber, M.E.: Bubbles, Drops, and Particles. Academic Press, 1978.

[5] Grace J.R.: Shapes and velocities of bubbles rising in infinite liquids. Trans. Instn. Chem. Eng. 51 (1973) 116-120.

[6] Juncu, Gh.: A numerical study of steady viscous flow past a fluid sphere. Int. J. Heat Fluid Flow 20 (1999) 414-421.

[7] Marrucci, G., Apuzzo, G., Astarita, G.: Motion of Liquid Drops in Non-Newtonian Systems. AIChE Journal 16 (1970) 538-541.

[8] Mendelson, H.D.: The prediction of Bubble Terminal Velocities from Wave Theory. AIChE Journal 13 (1967) 250-253.

[9] Sabisch, W.: Dreidimensional numerische Simulation der Dynamik von aufsteigenden Einzelblasen und Blasenschwärmen mit einer Volume-of-Fluid Methode. Forschungszentrum Karlsruhe, Wissenschaftliche Berichte FZKA 6478, June 2000 (http://hikwww4.fzk.de/hbk/literatur/FZKA_Berichte/FZKA6478.pdf).

[10] Sabisch, W., Wörner, M., Grötzbach, G., Cacuci, D.G.: Dreidimensionale numerische Simulation von aufsteigenden Einzelblasen und Blasenschwärmen mit einer Volume-of-Fluid-Methode. Chemie-Ingenieur-Technik 73 (2001) 368-373.

[11] Sabisch, W., Wörner, M., Grötzbach, G., Cacuci, D.G.: 3D volume-of-fluid simulation of a wobbling bubble in a gas-liquid system of low Morton number. Proc. 4th Int. Conf. on Multiphase Flow (ICMF), New Orleans, LA, U.S.A., May 27 - June 1, 2001, CD-ROM, paper 244.

[12] Sussman, M., Puckett, E.G.: A Coupled Level Set and Volume-of-Fluid Method for Computing 3D and Axisymmetric Incompressible Two-Phase Flows. J. Comput. Phys. 162 (2000) 301-337.

[13] Tomiyama, A., Kataoka, I., Zun, I., Sakaguchi, T.: Drag Coefficients of Single Bubbles under Normal and Micro Gravity Conditions. JSME International Journal Series B 41 (1998) 472-479.

[14] Wellek, R.M., Agrawal, A.K., Skelland, A.H.P.: Shape of liquid drops moving in liquid media. AIChE Journal 12 (1966) 854-862.

[15] Wörner, M., Sabisch, W., Grötzbach, G., Cacuci, D.G.: Volume-averaged conservation equations for volume-of-fluid interface tracking. Proc. 4th Int. Conf. on Multiphase Flow (ICMF), New Orleans, LA, U.S.A., May 27 - June 1, 2001, CD-ROM, paper 245.